# Polaron relaxation and charge dynamics near the mobility edge of a possible Wigner lattice of polarons

Gayan Prasad Hettiarachchi,[1,2,*] Yoshifumi Nishida,[2] and Yusuke Masaki[2]

[1]*Graduate School of Engineering Science, Osaka University, Toyonaka, Osaka 560-8531, Japan*
[2]*Department of Physics, Osaka University, Toyonaka, Osaka 560-0043, Japan*

We performed impedance spectroscopy and optical investigations below the reported mobility edge of two models systems ($X_n/X_{1.95-\delta}Al_{1.95}Si_{2.05}O_{8.00}$; $X$ = K or Rb, $n$ is the doping density of guest atoms) used to explore the metal-insulator transition in a deformable lattice. The bulk ac conductivity and imaginary dielectric permittivity of insulating samples near the mobility edge in both systems show a power-law behavior and variable-range hopping (VRH) conduction that is indeed related to the proposed polaron relaxation and conduction. We show that polaron relaxation and VRH occur simultaneously above a particular *density* of an interacting gas of small (bi)polarons, which is commensurate with the electron-lattice coupling strength and the intersite electron transfer energy. Based on our experimental results, we propose a rich phase diagram for the charge dynamics in a deformable lattice from the perspective of a Wigner lattice of small (bi)polarons.

## I. INTRODUCTION

There is considerable interest in the metal-insulator transition (MIT) in a deformable ionic lattice [1–5] because it has the potential to explain bizarre properties of disordered systems near the mobility edge and provide insight for solving the longstanding puzzle of Mooij correlations [6–8]. This has implications for many systems, such as manganites [9,10], perovskites [11], cuprates [12], conjugated polymers [13], and organic materials [14], where the nontrivial interplay of electron correlation, electron-lattice coupling, and disorder effects cannot be ignored. Theoretical studies investigating the effects of Anderson localization (both interacting and noninteracting scenarios) and finite electron-lattice coupling on electron transport in a polarizable ionic-lattice highlighted the opening of a mobility gap due to polaron formation [1,15,16]. The closing of this mobility gap with decreasing disorder in the electronic potential (the random electronic potential is abbreviated as $W$, hereafter) at fixed electron-lattice coupling strength $\lambda$ or with the weakening of $\lambda$ at fixed $W$ gives rise to a rich phase diagram and has been attributed to the nontrivial interactions in a many-polaron system and correlated response of $W$ to the lattice [1,3,4].

Recent experimental studies have used quasi-two-dimensional $X_{1.95-\delta}Al_{1.95}Si_{2.05}O_{8.00}$ (abbreviated as $X_2$-P; $X$ = Na, K, Rb, or Cs) as a model system to explore the MIT in a deformable ionic lattice because it allows the probing of electron-lattice coupling, electron-correlation effects, and the random electronic potential on the same footing [3,4,17]. Guest atoms were introduced into this system to modulate the density of ionized electronic-charge carriers. These charge carriers interact with $X$ inducing polaron effects leading to local lattice deformations. These deformations affect $W$, which can be controlled by modulating the guest-atom (electron)

density. The value of $\lambda$ can be controlled by changing the guest element. The optical and nonmagnetic properties of guest K atoms in $K_2$-P (abbreviated as $K_n/K_2$-P; $n$ is the average number of guest atoms per formula unit) at $n < 1.09$ [3] and guest Rb atoms in $Rb_2$-P ($Rb_n/Rb_2$-P) at $n < 0.89$ [4] have revealed the formation of small bipolarons that opens a mobility gap. Direct current (dc) transport measurements have shown a discontinuous and continuous closing of this gap with increasing $n$ in the K system (at $n = 1.09$) and the Rb system (at $n = 0.89$), respectively [3,4]. These reports have provided invaluable experimental evidence to reconcile two diverging theories discussing the MIT in a deformable lattice, one supporting a discontinuous transition [15,16] and the other a continuous transition [1] to extended states analogous to a disordered metal. Even though the transport properties below the mobility edge and the scaling of the (dis)continuity of the transition have been attributed to the nontrivial interplay of polaron correlation effects, dynamical lattice deformations, $W$, and $\lambda$, direct evidence remains elusive restricting an affirmative assignment to polaron relaxation and conduction below the mobility edge [1,15].

Impedance spectroscopy is ideal for gauging polaron effects and has been employed in a body of literature to observe polaron relaxation in a variety of materials [18–22]. For perovskite materials, polaron relaxation exists at low temperatures in crystals with disorder [18]. In perovskite-related material $CaCu_3Ti_4O_{12}$ [20], Fe-doped $SrTiO_3$ [19], $VO_2$ [22], and $LaMn_{1-x}Fe_xO_3$ [21], polaron relaxation has been found to be strongly linked to Mott's variable-range hopping (VRH) conduction [23,24]. Here, we use impedance spectroscopy to confirm the existence of polaron relaxation in $K_n/K_2$-P and $Rb_n/Rb_2$-P below the reported conducting transition [3,4]. We separate bulk and grain-boundary contributions and demonstrate that the bulk transport at the vicinity of the mobility edge can indeed be assigned to polaron relaxation and VRH of polarons. Well below the mobility edge, we observe a region
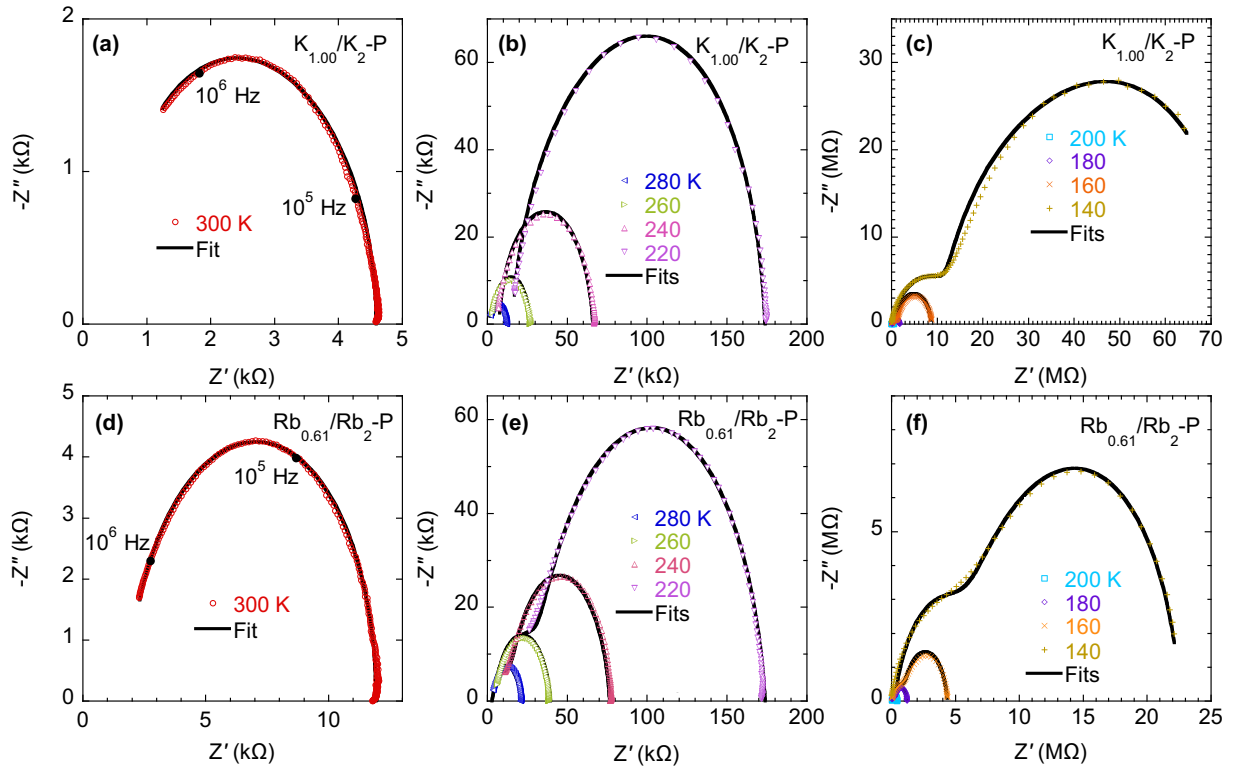
*hettiarachchi@hpr.stec.es.osaka-u.ac.jp

FIG. 1. The complex-impedance plane plots of $K_{1.00}/K_2$-P at (a) 300 K, (b) 280–220 K, and (c) 200–140 K and those of $Rb_{0.61}/Rb_2$-P at (d) 300 K, (e) 280–220 K, and (f) 200–140 K. The solid curves represent the fits of complex impedance using a model of two parallel resistance, $R$, and capacitance, $C$, elements connected in series.

demonstrating nearest-neighbor hopping (NNH) conduction, however, with no convincing evidence of polaron relaxation. This does not exclude polaron formation well below the mobility edge but suggests that polaron relaxation and VRH occur simultaneously above a particular *density* in an interacting gas of small (bi)polarons with decreasing $W$. This density is commensurate with $\lambda$ and the intersite electron transfer energy $t'$.

## II. EXPERIMENTAL

Powder samples of $K_n/K_2$-P ($n$ = 0.31, 0.39, 0.52, 0.62, 0.69, 0.90, 1.00, and 1.05) and $Rb_n/Rb_2$-P ($n$ = 0.29, 0.40, 0.52, 0.61, 0.70, and 0.81) were prepared by vapor adsorption of accurately weighed K into $K_2$-P and Rb into $Rb_2$-P inside sealed glass tubes at 150 and 100 °C, respectively. Details of the $X_2$-P structure can be found elsewhere [3,25]. Powder samples were pressed into pellets (diameter ≈4 and thickness ≈0.8 mm) with Au electrodes, and impedance measurements were performed over the frequency range 20 Hz to 2 MHz with an applied voltage of 500 mV using an Agilent 4824A LCR meter. Measurements were carried out in the temperature range 10–300 K using a physical property measurement system (Quantum Design). The diffuse reflectance $r(\omega)$ was measured at room temperature using an ultraviolet-visible near-infrared spectrometer and a Fourier transform infrared spectrometer. The optical absorption was obtained using the Kubelka-Munk transformation $k/s = (1 − r)^2/2r$ [26], where $k$ and $s$ are the absorption and scattering coefficients, respectively.

## III. RESULTS AND DISCUSSION

The impedance spectroscopy data of $K_n/K_2$-P at $n$ = 0.69, 0.90, 1.00, and 1.05 and $Rb_n/Rb_2$-P at $n$ = 0.40, 0.52, 0.61, 0.70, and 0.81 are modeled with two parallel resistance, $R$, and capacitance, $C$, elements connected in series representing the bulk and grain-boundary responses [27]. For $K_n/K_2$-P at $n$ = 0.31, 0.39, and 0.52 and $Rb_n/Rb_2$-P at $n$ = 0.29, the experimental values exceed the measurement limit indicating that these samples are deep in the insulating phase. For $K_n/K_2$-P at $n$ = 0.62, the impedance values are below the measurement limit only in a very limited region at high temperature. The complex-impedance plane plots of $K_{1.00}/K_2$-P and $Rb_{0.61}/Rb_2$-P representative of $K_n/K_2$-P at $n \geqslant 0.69$ and $Rb_n/Rb_2$-P at $n \geqslant 0.40$ are shown in Figs. 1(a)–1(f). At 300 K, $K_{1.00}/K_2$-P contains an arc with a nonzero intercept at high frequencies as shown in Fig. 1(a). The position of the arc in the frequency spectrum depends on the relaxation time $\tau$, and in general, $\tau$ for grain-boundary regions is much larger and is relaxed at lower frequencies than for bulk effects. Based on an equivalent circuit consisting of two parallel $RC$ elements connected in series the nonzero intercept indicates the presence of an arc with maximum angular frequency $\omega_m$ ($\omega = 2\pi f$; $f$ is the measured frequency) higher than 2 MHz. For this component $R$ is 400 $\Omega$. The large arc has $R \approx 4600 \Omega$ at 20 Hz and $C \approx 60$ pF. Room-temperature data indicates that $K_{1.00}/K_2$-P consists of semiconducting grains (bulk resistance $R_b \approx 400 \Omega$) and moderately insulating grain boundaries (grain-boundary resistance $R_{gb} \approx 4600 \Omega$). $K_{1.00}/K_2$-P shows
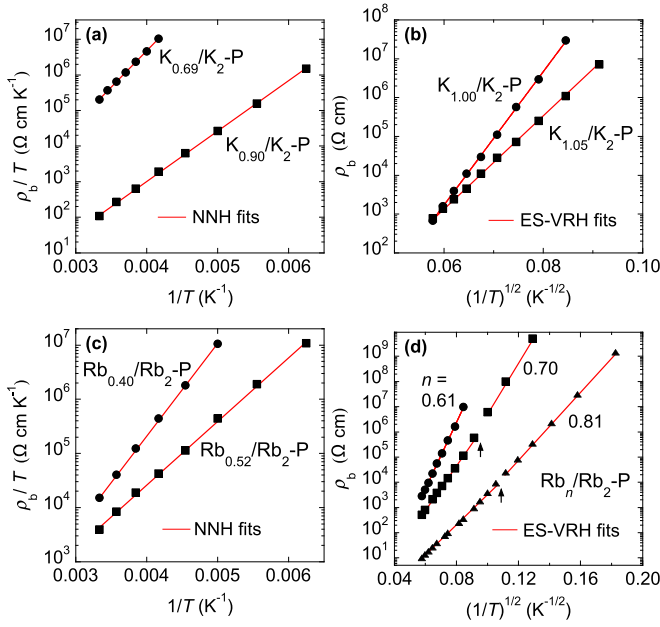
FIG. 2. The temperature dependence of the bulk resistivity $\rho_b$ of (a) $K_n/K_2$-P at $n = 0.69$ and $0.90$ fit with adiabatic nearest-neighbor hopping (NNH), (b) at $n = 1.00$ and $1.05$ fit with the variable-range hopping model of Efros and Shklovskii (ES-VRH) given by Eq. (1), (c) $Rb_n/Rb_2$-P at $n = 0.40$ and $0.52$ fit with NNH, and (d) at $n = 0.61$, $0.70$ and $0.81$ fit with ES-VRH. The arrows in panel (d) indicate the change of the gradient in the ES-VRH fits. The solid straight lines are fits of the respective models.

a large arc with a nonzero intercept down to 220 K as shown in Fig. 1(b). A trace of the expected high-frequency arc pertaining to the bulk is observed below 200 K as seen in Fig. 1(c). At 140 K, $R_b$ and $R_{gb}$ are approximately 19 and 75 M$\Omega$, respectively, and only part of the grain-boundary arc is observed above 20 Hz. Using the same approach, $R_b$ and $R_{gb}$ are extracted for $K_n/K_2$-P at $n = 0.69$, $0.90$, and $1.05$ and also for $Rb_n/Rb_2$-P at $n = 0.40$, $0.52$, $0.61$, $0.70$, and $0.81$. Representative plots of $Rb_{0.61}/Rb_2$-P are shown in Figs. 1(d)–1(f).

The temperature dependence of the grain-boundary resistivity $\rho_{gb}$ of $K_n/K_2$-P and $Rb_n/Rb_2$-P can be modeled with an activation process (not shown here) given by $\rho \propto \exp(E_a/k_BT)$, where $E_a$ is the activation energy and $k_B$ is the Boltzmann constant. Since our primary concern is to understand the conduction mechanism in the bulk, we do not resort to an extensive analysis of the grain-boundary contribution. The bulk resistivities $\rho_b$ of $K_n/K_2$-P at $n = 0.69$ and $0.90$ and $Rb_n/Rb_2$-P at $n = 0.40$ and $0.52$ yield best fits to adiabatic NNH, $\rho \propto T \exp(E_a/k_BT)$, as shown in Figs. 2(a) and 2(c), respectively. The estimated values of $E_a$ are given in Table I. For $K_n/K_2$-P at $n = 1.00$ and $1.05$ and for $Rb_n/Rb_2$-P at $n = 0.61$, $0.70$, and $0.81$, $\rho_b$ does not follow $T^{-1}$ laws characteristic of activation or NNH. Further, these samples cannot be fit with Mott's VRH model proposed for noninteracting carriers [23,24], $\rho \propto \exp(T_0/T)^\nu$, where $\nu = 1/4$ or $1/3$ for a three-dimensional or a two-dimensional system, respectively; $T_0 = 24/[\pi k_B N(E_F)\xi^3]$ is a parameter related to the density of localized states at the Fermi level $N(E_F)$; and $\xi$ is the decay

length of the localized wave function associated with the charge carriers. The VRH model of Efros and Shklovskii (ES-VRH) incorporating electron-electron interactions [28,29],

$$\rho \propto \exp\left(\frac{T^*}{T}\right)^{\frac{1}{2}}, \qquad (1)$$

where $T^* = 2.8e^2/[4\pi\varepsilon_0\varepsilon k_B\xi]$, $\varepsilon_0$ is the permittivity of the vacuum, and $\varepsilon$ is the dielectric constant of the material, yields better fits to $K_n/K_2$-P at $n = 1.00$ and $1.05$ and $Rb_n/Rb_2$-P at $n = 0.61$, $0.70$, and $0.81$ as shown in Figs. 2(b) and 2(d), respectively. The estimated values of $T^*$ and $\xi$ are given in Table I. The estimated values of $\xi$ suggest that for $K_{1.00}/K_2$-P and $K_{1.05}/K_2$-P the wave function of electrons extends to adjacent cages (the unit cell comprises four cages with lattice constants $a \approx 14$ and $b \approx c \approx 10$ Å [3,25]). For $Rb_{0.70}/Rb_2$-P and $Rb_{0.81}/Rb_2$-P the wave function extends to several cages. At $100 \sim 120$ K, the gradient of the ES-VRH fitting changes [marked by the arrows in Fig. 2(d)], indicating an increase in $\xi$ for these two samples at high temperature.

The frequency dependence of the ac conductivity $\sigma$ is shown in Figs. 3(a) and 3(c) for $K_{1.00}/K_2$-P and $Rb_{0.61}/Rb_2$-P, respectively, at temperatures for which the bulk arc is observed in the complex-impedance plane plots [see Figs. 1(c) and 1(f)]. The experimental curves show two or three ranges of behavior depending on the temperature. First, there is a strong rise at low frequencies. This is the grain-boundary blocking effect. Second, $\sigma$ does not increase as rapidly at high frequency. It is the bulk conductivity relaxation which is of primary interest. The relaxation frequency $f_r$ is marked by the arrows in Fig. 3. This behavior can be described by the universal dielectric response (UDR) [30,31],

$$\sigma = \sigma_{dc} + \sigma_0 f^s, \qquad (2)$$

where $\sigma_{dc}$ is the bulk dc conductivity, $\sigma_0$ is a constant, and $s$ ($<1$) is an exponent describing a power-law behavior. The UDR is typical of thermal-assisted tunneling between localized states. The fits representing this behavior are shown by the solid curves in Figs. 3(a) and 3(c). The value of $s$ decreases with temperature as shown in Figs. 3(e) and 3(f) for $K_{1.00}/K_2$-P and $Rb_{0.61}/Rb_2$-P, respectively. For correlated hopping between localized sites over a potential barrier, the value of $s$ is predicted to decrease with temperature [32]. At sufficiently high frequency and low temperature, a crossover from the power law to a linear increase, $\sigma \propto f$ defined as the second universality (SU), is observed [21,31,33,34]. Fitting of this behavior is shown by the broken lines in Figs. 3(a) and 3(c). The microscopic origin of the SU region is not clearly understood. The UDR and the SU are also observed in limited temperature ranges for $K_n/K_2$-P at $n = 0.69$, $0.90$, and $1.05$, and for $Rb_n/Rb_2$-P at $n = 0.40$, $0.52$, $0.70$, and $0.81$ (not shown here).

For polaron relaxation the frequency variation of the imaginary dielectric permittivity $\varepsilon''$ follows a fractional power law, $\varepsilon'' \propto f^{s-1}$ above $f_r$ [20,21]. We observe this behavior for $K_n/K_2$-P at $n = 1.00$ and $1.05$ and for $Rb_n/Rb_2$-P at $n = 0.61$, $0.70$, and $0.81$. The fitting of $\varepsilon'' \propto f^{s-1}$ is shown in Figs. 3(b) and 3(d) for $K_{1.00}/K_2$-P and $Rb_{0.61}/Rb_2$-P, respectively. The exponent $s$ is comparable with the value obtained from fitting the UDR. Therefore, the high-frequency behavior ($f > f_r$) of $\sigma$ and $\varepsilon''$ pertaining to the bulk of $K_n/K_2$-P at $n \geqslant 1.00$

TABLE I. The parameters used to fit adiabatic nearest-neighbor and variable-range hopping on the bulk electrical resistivity and small-polaron absorption spectrum on the absorption spectra of $K_n/K_2$-P and $Rb_n/Rb_2$-P.

| Sample | $E_a$ (eV) | $T^*$ (K) | $\xi$ (Å) | $E_b$ (eV) |
|---|---|---|---|---|
| $K_{0.31}/K_2$-P | | | | $0.70 \pm 0.02$ |
| $K_{0.39}/K_2$-P | | | | $0.68 \pm 0.03$ |
| $K_{0.69}/K_2$-P | $0.38 \pm 0.02$ | | | $0.70 \pm 0.02$ |
| $K_{0.90}/K_2$-P | $0.27 \pm 0.01$ | | | $0.69 \pm 0.01$ |
| $K_{1.00}/K_2$-P | | $1.57 \times 10^5$ | 6 | $0.70 \pm 0.03$ |
| $K_{1.05}/K_2$-P | | $7.6 \times 10^4$ | 7 | $0.68 \pm 0.02$ |
| $Rb_{0.29}/Rb_2$-P | | | | $0.61 \pm 0.01$ |
| $Rb_{0.40}/Rb_2$-P | $0.33 \pm 0.03$ | | | $0.62 \pm 0.02$ |
| $Rb_{0.52}/Rb_2$-P | $0.23 \pm 0.02$ | | | $0.62 \pm 0.01$ |
| $Rb_{0.61}/Rb_2$-P | | $9.2 \times 10^4$ | 6 | $0.60 \pm 0.02$ |
| $Rb_{0.70}/Rb_2$-P | | $3.2 \times 10^4 (\gtrsim 120 K); 5.9 \times 10^4 (\lesssim 120 K)$ | $10 (\gtrsim 120 K); 7 (\lesssim 120 K)$ | $0.63 \pm 0.01$ |
| $Rb_{0.81}/Rb_2$-P | | $1.6 \times 10^4 (\gtrsim 100 K); 2.8 \times 10^4 (\lesssim 100 K)$ | $24 (\gtrsim 100 K); 16 (\lesssim 100 K)$ | $0.61 \pm 0.02$ |

and $Rb_n/Rb_2$-P at $n \geqslant 0.61$ are consistent with the UDR and polaron relaxation. We do not observe convincing evidence of polaron-relaxation behavior in $K_n/K_2$-P for $n < 1.00$ and $Rb_n/Rb_2$-P for $n < 0.61$. The fitting of $\varepsilon'' \propto f^{s-1}$ in the frequency region demonstrating UDR in these samples renders a large error.

The electric modulus corresponds to the relaxation of the electric field in the material when the electric displacement remains constant. Hence, the electric modulus represents the dielectric relaxation process and is widely used to study conductivities of materials [21]. The complex electric modulus $M^*$ is given by $M^* = M' + iM''$, where $M'$ and $M''$ are the real and imaginary parts of the electric modulus. The variation of $M''$ as a function of frequency at different temperatures provides useful information about the charge transport mechanism and conductivity relaxation process. $M^*$ can be expressed as

$$M^*(\omega) = M_\infty \left[ 1 - \int_0^\infty \left( \frac{-d\phi(t)}{dt} \right) \exp(-i\omega t) dt \right], \quad (3)$$

where $M_\infty$ is the asymptotic value of $M'(\omega)$, $\phi(t) = \exp[-(t/\tau_M)^\beta]$ represents the time evolution of the electric field within the material [35], $\beta$ $(0 < \beta < 1)$ is the stretched exponent, and $\tau_M$ is the conductivity relaxation time. Peaks are observed in the frequency spectra of $M''$ in limited temperature ranges, which indicate the existence of a conductivity relaxation process. The frequencies at which the peaks in $M''$ are observed follow the relation $\omega_{max}\tau_M = 1$, where $\omega_{max}$ is the angular frequency corresponding to the peak maximum. In a limited temperature range, it is typically observed that $\tau_M$ follows the Arrhenius behavior given by

$$\tau_M = \tau_{M0}\exp(E_{Ma}/k_B T), \quad (4)$$

where $\tau_{M0}$ is the pre-exponential factor and $E_{Ma}$ is the activation energy. Figures 4(a) and 4(b) show the variation of $M''$ with frequency at different temperatures for $K_{1.05}/K_2$-P and $Rb_{0.70}/Rb_2$-P, respectively, representative of samples that show polaron relaxation ($K_n/K_2$-P at $n \geqslant 1.00$ and $Rb_n/Rb_2$-P at $n \geqslant 0.61$). Peaks in $M''$ are observed in the measured frequency region only in a limited temperature range. We fit the variation of $\tau_M$ obtained from the peak frequencies with the Arrhenius behavior given by Eq. (4), and the fits

are shown by the solid straight lines in Fig. 4(c). The $E_{Ma}$ values obtained from fitting are 0.17 eV for $K_{1.05}/K_2$-P, 0.11 eV for $Rb_{0.70}/Rb_2$-P, and 0.05 eV for $Rb_{0.81}/Rb_2$-P. The values of $\tau_{M0}$ are $5.9 \times 10^{-13}$ s for $K_{1.05}/K_2$-P, $4.3 \times 10^{-12}$ s for $Rb_{0.70}/Rb_2$-P, and $4.2 \times 10^{-11}$ s for $Rb_{0.81}/Rb_2$-P. For comparison, values between $10^{-10} \sim 10^{-14}$ s are reported for materials exhibiting polaron relaxation [21,36,37]. Although $K_{1.00}/K_2$-P and $Rb_{0.61}/Rb_2$-P show polaron relaxation [see Figs. 3(b) and 3(d)], peaks in $M''$ are observed in a very limited temperature range rendering it impossible to perform a similar analysis for these two samples.

The scaling of the electric modulus can give further information about the evolution of the relaxation dynamics, structure, and concentration of charge carriers. Figure 4(d) shows the scaling results at different temperatures for representative $Rb_{0.70}/Rb_2$-P, where $M''_{max}$ and $\omega_{max}$ are used as the scaling parameters for $M''$ and $\omega$, respectively. All modulus spectra overlap and are scaled to a single master curve in the low-frequency region, while deviations are observed in the high-frequency region. Deviations in the high-frequency region occur due to changes in the dynamical properties of the sample [21]. This could be indicative of the change in $\xi$ observed around 100 K for $Rb_{0.70}/Rb_2$-P and $Rb_{0.81}/Rb_2$-P [see Fig. 2(d) and Table I]. It is also noted that this could be indicative of an increase in the concentration of the temperature-activated charge carriers around 100 K. In either case, dynamical changes in the polaron relaxation process are seen around 100 K. However, the physics underlying this behavior is unclear and would require investigations of the local structures and any dynamical lattice deformations/relaxations with temperature.

Representative room-temperature optical absorption spectra of $K_n/K_2$-P at $n = 0.31$, 0.39, and 1.00 and $Rb_n/Rb_2$-P at $n = 0.29$, 0.40, and 0.61 are shown in Figs. 5(a) and 5(b), respectively. Similar to previous reports [3,4], bands are observed at approximately 10 600 $cm^{-1}$ for $K_n/K_2$-P and 9000 $cm^{-1}$ for $Rb_n/Rb_2$-P (solid circles) that may be attributed to excitations of self-trapped states. The small-polaron absorption spectrum $\alpha_{sp}$ is given by [38,39]

$$\alpha_{sp}(\omega) = \frac{2(\pi)^{3/2}e^2}{m^*\omega c} \frac{t'}{\Delta} \exp\left[ -\frac{(2E_b - \hbar\omega)^2}{\Delta^2} \right], \quad (5)$$
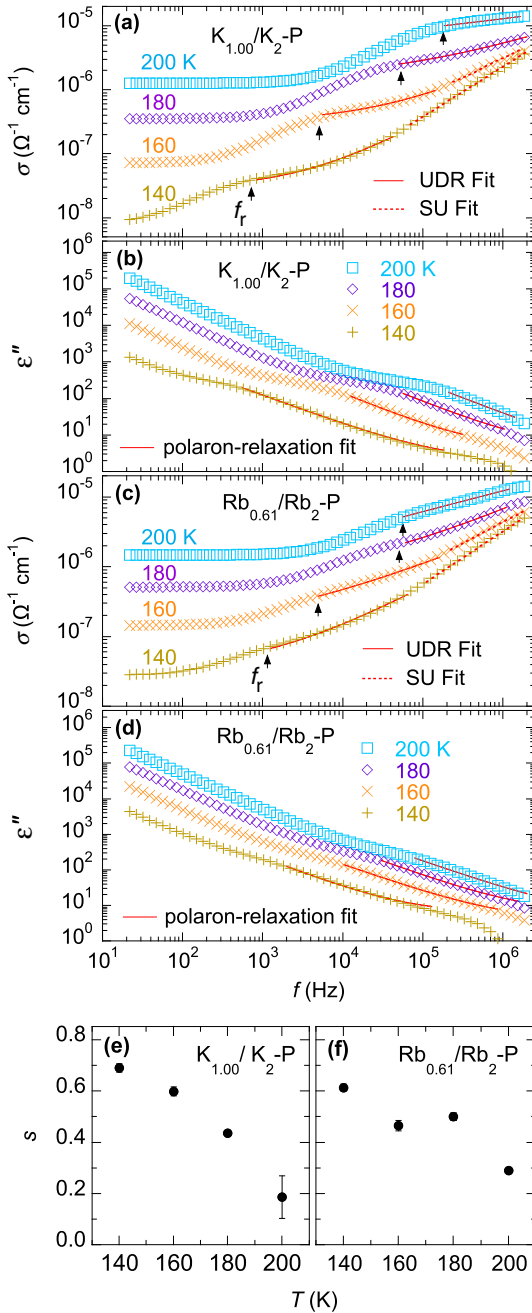
FIG. 3. The frequency dependence of the ac conductivity $\sigma$ of (a) $K_{1.00}/K_2$-P and (c) $Rb_{0.61}/Rb_2$-P and the imaginary dielectric permittivity $\varepsilon''$ of (b) $K_{1.00}/K_2$-P and (d) $Rb_{0.61}/Rb_2$-P. The solid curves and broken straight lines in panels (a) and (c) are the fits of the universal dielectric response (UDR) given by Eq. (2) and the second universality, respectively. The solid curves in panels (b) and (d) are the fits of polaron relaxation. The exponent $s$ extracted from fitting the UDR on (e) $K_{1.00}/K_2$-P and (f) $Rb_{0.61}/Rb_2$-P.



FIG. 4. The frequency dependence of the imaginary part of the electric modulus $M''$ of (a) $K_{1.05}/K_2$-P from 80 to 180 K and (b) $Rb_{0.70}/Rb_2$-P from 40 to 140 K. (c) The extracted conductivity relaxation time $\tau_M$ against $T^{-1}$ for $K_{1.05}/K_2$-P, $Rb_{0.70}/Rb_2$-P, and $Rb_{0.81}/Rb_2$-P. The solid straight lines are the best fits of Eq. (4). (d) Scaling of the electric modulus for $Rb_{0.70}/Rb_2$-P at different temperatures.

where $m^*$ is the effective electronic mass, $c$ is the speed of light, $t' \equiv \hbar^2/2m^*a^2$, $\hbar$ is the reduced Planck-constant, $a$ is a lattice constant, $E_b$ is the small-polaron binding energy, $\Delta \equiv \sqrt{8E_bE_{vib}}$, and $E_{vib}$ is the characteristic vibrational energy ($\approx k_BT$ at room temperature). The $\alpha_{sp}(\omega)$ term gives the absorption coefficient per unit small-polaron *density*. A small polaron exhibits an asymmetric absorption at the reso-
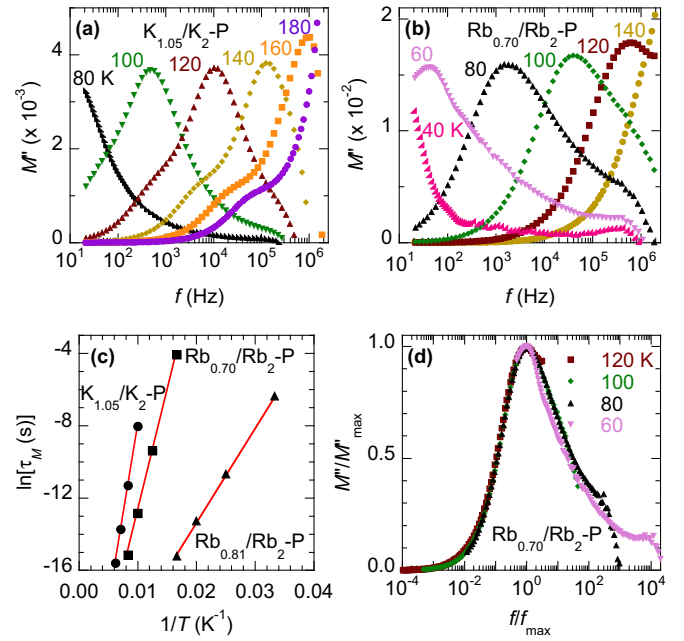
nant excitation energy $\hbar\omega = 2E_b$ [39]. For an intrasite small bipolaron, the excitation energy is $4E_b - U$, where $U$ is the on-site Coulomb repulsion energy [39,40]. In this case, $U$ is very large ($>5$ eV) and is in the strongly-correlated regime [41]. The small bipolarons in these systems are proposed to be intersite [3,4], i.e., weakly coupled states of two small polarons at adjacent sites, in effect minimizing $U$. Hence, we use the small-polaron absorption spectrum given by Eq. (5) to fit the absorption spectra. The curves represented by the broken lines are the fits of Eq. (5) on the bands at approximately 10 600 $cm^{-1}$ of $K_n/K_2$-P and 9000 $cm^{-1}$ of $Rb_n/Rb_2$-P. The values of $E_b$ obtained from fitting are summarized in Table I.

From the perspective of a two-site model, the absorption bands of $K_n/K_2$-P at approximately 10 600 $cm^{-1}$ and $Rb_n/Rb_2$-P at 9000 $cm^{-1}$ with the resonant excitation energy $\hbar\omega$ can be viewed as Franck-Condon-like excitations with two relaxation paths leading to either an on-site relaxation or a hopping transfer as indicated by paths I and II in Fig. 6, respectively [42,43]. Since these absorptions become evident in $K_n/K_2$-P and $Rb_n/Rb_2$-P from very low values of $n$, where no traces of conductivity are observed in the transport properties, we conjecture that these are indicative of on-site excitations and relaxations. The value of $E_a$ is related to $E_b$ by $E_a \approx \frac{1}{2}E_b - J$, where $J$ is the electronic overlap integral between two adjacent sites [44]. This relationship is approximately satisfied by $K_{0.69}/K_2$-P, $K_{0.90}/K_2$-P, $Rb_{0.40}/Rb_2$-P, and $Rb_{0.52}/Rb_2$-P (see Table I). However, $K_{0.90}/K_2$-P and $Rb_{0.52}/Rb_2$-P show a decrease in $E_a$, while $E_b$ remains constant. This may be attributed to the increase in $J$ with the increasing number density of small bipolarons, especially above the percolation
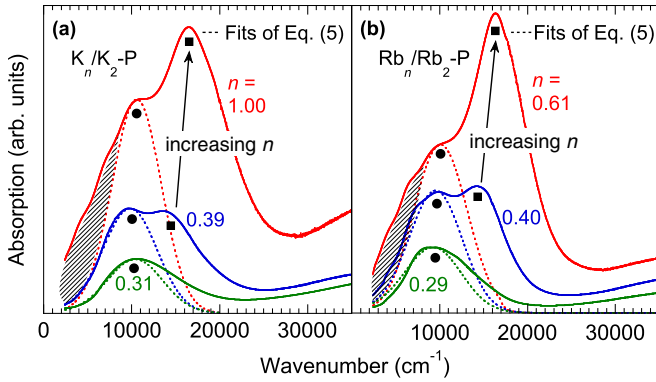
FIG. 5. The room-temperature optical absorption spectra of (a) $K_n/K_2$-P at $n = 0.31$, 0.39, and 1.00 and (b) $Rb_n/Rb_2$-P at $n = 0.29$, 0.40, and 0.61. The solid circle and square mark the small bipolaron and high-frequency bands, respectively. The broken curves are the fits of the small-polaron absorption spectrum given by Eq. (5) on the bands at approximately 10 600 and 9000 $cm^{-1}$ of $K_n/K_2$-P and $Rb_n/Rb_2$-P, respectively. The shaded spectral-areas of $K_{1.00}/K_2$-P, $Rb_{0.40}/Rb_2$-P, and $Rb_{0.61}/Rb_2$-P mark the midinfrared absorptions.

threshold, which will be discussed later. It is noted that the relationship between $E_a$ and $E_b$ can be very complicated due to the interplay of a multitude of parameters such as the random electronic potential, the distance between hopping sites, the transfer integral, etc., that change with doping. In some cases, the temperature-activated hopping energy practically drops to zero while the excitation energy at $\hbar\omega$ remains invariant [44]. This behavior was observed in $K_n/K_2$-P and $Rb_n/Rb_2$-P close to the mobility edge (not discussed here), however, with a drop in the intensity of the small bipolaron absorption band, which may be indicative of melting of small bipolarons at high density [3,4].

Increasing intensity of the small bipolaron bands at constant excitation energy suggests an increase in the density of small bipolarons with increasing $n$. At $n \approx 0.4$, in $K_n/K_2$-P and $Rb_n/Rb_2$-P, a new high-frequency (HF) band appears (solid squares) around 14 000 and 14 500 $cm^{-1}$, respectively. This band shows a blue-shift and increases in intensity with $n$. This
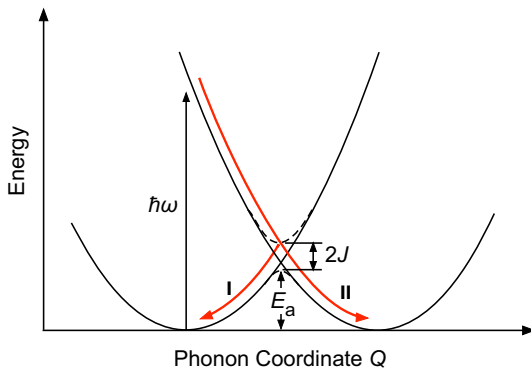


FIG. 6. The small polaron excitations in a two-site model in the adiabatic limit. The Franck-Condon-like excitations at $\hbar\omega$ lead to two relaxation paths: (I) on-site relaxation and (II) hopping transfer.

change in the absorption spectrum at $n \approx 0.4$, which is common to both systems, is perhaps triggered by the percolation of small bipolarons within the diamond lattice formed by the cage voids of the $X_2$-P framework [3,4,45]. The percolation threshold $P_c$ proposed for paired constituents in a diamond lattice is 0.35 [45]. In this scenario, the HF band can be attributed to the surface-plasmon excitations in the two-dimensional slabs of the framework [3], which is triggered by the many-polaron effect at percolation. Details can be found elsewhere [3,4]. The percolation of small bipolarons results in an array of interacting small bipolarons, which can be viewed in terms of a Wigner lattice of polarons (PWL) [46,47]. A further increase in $n$ ($>0.4$), i.e., increasing number density of small bipolarons above $P_c$, is analogous to an increase in the density of a PWL [46–48].

The electron-lattice coupling induces incoherent contributions generating multiphonon absorption bands in the mid-infrared (MIR) region [4,49–51]. The shaded spectral-areas in the low-frequency region of $K_{1.00}/K_2$-P, $Rb_{0.40}/Rb_2$-P, and $Rb_{0.61}/Rb_2$-P mark the MIR absorptions. The spectral area in the low-frequency region not covered by the small bipolaron absorption band becomes quite discernible in $Rb_n/Rb_2$-P at $n = 0.40$ following percolation simultaneously with the appearance of NNH conduction [see Fig. 2(c)]. For $K_n/K_2$-P, this becomes evident at a much larger value of $n = 0.69$ (not shown here) simultaneously with the appearance of NNH [see Fig. 2(a)]. The spectral area of the MIR absorptions grows with increasing $n$ in $K_n/K_2$-P and $Rb_n/Rb_2$-P. In this scenario, the MIR absorptions are attributed to photoinduced hopping (nearest neighbor or variable range) of small bipolarons.

Below $P_c$, $K_n/K_2$-P and $Rb_n/Rb_2$-P are deep within the insulating phase due to isolated small bipolarons. This is confirmed by the high-resistivity values (above the measurement limit) observed for $K_n/K_2$-P at $n = 0.31$ and 0.39 and $Rb_n/Rb_2$-P at $n = 0.29$. At percolation ($n \approx 0.4$), $Rb_n/Rb_2$-P enters a NNH region [see Fig. 2(c)]. The percolation results in an array of interacting small bipolarons, likely a PWL, with temperature-activated hopping between adjacent sites in a limited high-temperature region (200 ∼ 300 K). With increasing small bipolaron density, $Rb_n/Rb_2$-P enters a region that demonstrates VRH and polaron relaxation at $n = 0.61$ [see Figs. 2(d) and 3(d)]. Increasing density in a PWL can relax the initial lattice deformations and, in turn, weaken $W$, giving rise to VRH of polarons in an extended temperature range [46,48]. This behavior continues up to the mobility edge around which a continuous transition to extended states was reported at $n = 0.89$ [4]. A phase diagram summarizing the evolution of the charge dynamics pertaining to $Rb_n/Rb_2$-P (solid squares) is shown in Fig. 7.

In contrast to $Rb_n/Rb_2$-P, the percolation of small bipolarons at $n \approx 0.4$ does not give rise to NNH in $K_n/K_2$-P. It remains a stubborn insulator. One possible factor contributing to this behavior is the stronger $\lambda$ of K, which creates a comparatively deeper deformation potential that restrains temperature-activated behavior. However, interestingly, $E_b$ estimated for $K_n/K_2$-P is not significantly larger than that of $Rb_n/Rb_2$-P (see Table I). Another factor that comes into play is the $4s$ electron wave-function, which is less spread in comparison to the $5s$ electron wave-function of Rb, resulting in a smaller $t'$ or $J$. At $n = 0.62$, resistivity below the measurement limit is
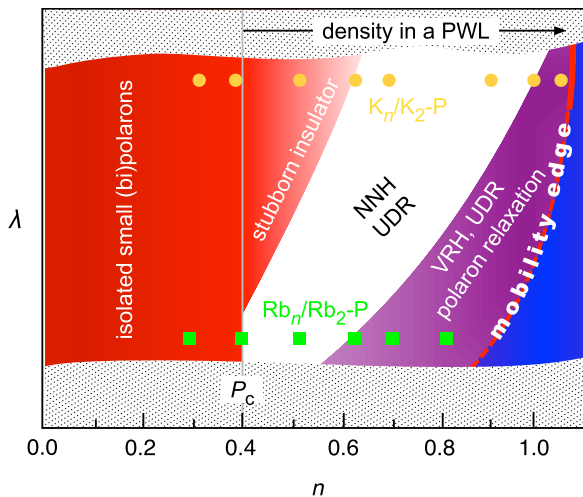
FIG. 7. The phase diagram depicting the charge dynamics in a deformable lattice from the perspective of an interacting gas of small (bi)polarons. See the text for details.

observed, however, in a very limited high-temperature region. Subsequently, NNH is observed at $n = 0.69$ in a temperature range wide enough to perform fitting [see Fig. 2(a)]. It is observed that NNH appears at a comparably larger density in the PWL in the case of $K_n/K_2$-P. At $n = 1.00$, at high density and immediately below the reported mobility edge [3], VRH and polaron relaxation are observed in $K_n/K_2$-P [see Figs. 2(b) and 3(b)]. This behavior continues in the insulating samples of $K_n/K_2$-P up to the mobility edge, at which a discontinuous transition to extended states was reported at $n = 1.09$ [3]. The microscopic mechanism at work behind this discontinuity is not understood. The evolution of the charge dynamics pertaining to $K_n/K_2$-P is also shown in Fig. 7 (solid circles). The discontinuity of the reported transition [3] is illustrated by changing the broken red line denoting the mobility edge to a solid line. The hatched regions in Fig. 7 at stronger and weaker $\lambda$ are yet to be explored using impedance spectroscopy.

Although the optical properties suggest the formation of small bipolarons from very low values of $n$, both $K_n/K_2$-P and

$Rb_n/Rb_2$-P provide no convincing evidence of polaron relaxation and hopping for samples deep within the insulating phase. The small bipolarons are isolated below $P_c$, and we conjecture that for NNH conduction of polarons, realization of an array of interacting small (bi)polarons through percolation is a necessity. At comparatively weaker $\lambda$ and larger $t'$, this condition is sufficient as observed for $Rb_n/Rb_2$-P. However, for stronger $\lambda$, it is not; NNH appears at a higher density as observed for $K_n/K_2$-P possibly due to an increase in $J$ and readjustments in the electronic potential. Polaron relaxation and VRH becomes evident simultaneously after a region of NNH with a further increase in the density, which is clearly commensurate with $\lambda$ and $J(t')$.

In summary, we performed impedance spectroscopy and optical measurements of two model systems used to investigate the metal-insulator transition in a deformable lattice. The bulk conductivity immediately below the mobility edge indeed shows a region demonstrating polaron relaxation and variable-range hopping conduction. Below this region and above the percolation threshold for small bipolarons, we observe a region demonstrating nearest-neighbor hopping conduction. Below the percolation threshold, isolation of small bipolarons suppress any form of hopping conduction. We show that the charge dynamics of an interacting gas of small (bi)polarons is strongly dependent on the density, the electron-lattice coupling strength, and the intersite electron transfer energy (or the electronic overlap integral between adjacent sites). We propose a phase diagram based on our experimental results, which has many implications for bizarre properties of disordered systems, transport near the mobility edge, and Mooij correlations.

[1] D. Di Sante, S. Fratini, V. Dobrosavljević, and S. Ciuchi, Phys. Rev. Lett. **118**, 036602 (2017).

[2] C. K. Lee, J. Moix, and J. Cao, J. Chem. Phys. **142**, 164103 (2015).

[3] G. P. Hettiarachchi, T. Nakano, Y. Masaki, M. N. Mohd Muhid, H. Hamdan, and Y. Nozue, J. Phys. Soc. Jpn. **84**, 014702 (2015).

[4] G. P. Hettiarachchi, F. Moriasa, Y. Nishida, T. Nakano, M. N. Mohd Muhid, and H. Hamdan, Phys. Rev. B **96**, 155115 (2017).

[5] G. P. Hettiarachchi, M. N. Mohd Muhid, and H. Hamdan, Phys. Rev. B **97**, 155142 (2018).

[6] P. A. Lee and T. V. Ramakrishnan, Rev. Mod. Phys. **57**, 287 (1985).

[7] J. H. Mooij, Phys. Status Solidi A **17**, 521 (1973).

[8] M. Jonson and S. M. Girvin, Phys. Rev. Lett. **43**, 1447 (1979).

[9] H. M. Rønnow, C. Renner, G. Aeppli, T. Kimura, and Y. Tokura, Nature (London) **440**, 1025 (2006).

[10] A. J. Millis, Nature (London) **392**, 147 (1998).

[11] M. Bonn, K. Miyata, E. Hendry, and X.-Y. Zhu, ACS Energy Lett. **2**, 2555 (2017).

[12] D. Emin, *Polarons* (Cambridge University, Cambridge, England, 2013).

[13] L. Yu, *Solitons and Polarons in Conducting Polymers* (World Scientific, Singapore, 1988).

[14] E. Romero, R. Augulis, V. I. Novoderezhkin, M. Ferretti, J. Thieme, D. Zigmantas, and R. van Grondelle, Nat. Phys. **10**, 676 (2014).

[15] M. H. Cohen, E. N. Economou, and C. M. Soukoulis, Phys. Rev. Lett. **51**, 1202 (1983).

[16] M. H. Cohen, E. N. Economou, and C. M. Soukoulis, Phys. Rev. B **29**, 4496 (1984).

[17] T. Nakano and Y. Nozue, Adv. Phys.: X **2**, 254 (2017).

[18] O. Bidault, M. Maglione, M. Actis, M. Kchikech, and B. Salce, Phys. Rev. B **52**, 4191 (1995).

[19] C. Ang, Z. Yu, Z. Jing, P. Lunkenheimer, and A. Loidl, Phys. Rev. B **61**, 3922 (2000).

[20] L. Zhang and Z.-J. Tang, Phys. Rev. B **70**, 174306 (2004).

[21] A. Karmakar, S. Majumdar, and S. Giri, Phys. Rev. B **79**, 094406 (2009).

[22] X. Zhong, P. LeClair, S. K. Sarker, and A. Gupta, Phys. Rev. B **86**, 094114 (2012).

[23] N. F. Mott, J. Non-Cryst. Solids **1**, 1 (1968).

[24] N. F. Mott and E. A. Davis, *Electronic Proceeses in Non-crystalline Materials* (Clarendon, Oxford, 1979).

[25] B. R. Albert, A. K. Cheetham, J. A. Stuart, and C. J. Adams, Microporous Mesoporous Mater. **21**, 133 (1998).

[26] P. Kubelka and F. Munk, Z. Tech. Phys. **12**, 593 (1931).

[27] J. T. S. Irvine, D. C. Sinclair, and A. R. West, Adv. Mater. **2**, 132 (1990).

[28] A. L. Efros and B. I. Shklovskii, J. Phys. C: Solid State Phys. **8**, L49 (1975).

[29] D. N. Tsigankov and A. L. Efros, Phys. Rev. Lett. **88**, 176602 (2002).

[30] S. R. Elliott, Adv. Phys. **36**, 135 (1987).

[31] A. K. Jonscher, *Dielectric Relaxation in Solids* (Chelsea Dielectrics, London, 1983).

[32] J. Giuntini, B. Deroide, P. Belougne, and J. Zanchetta, Solid State Commun. **62**, 739 (1987).

[33] W. K. Lee, J. F. Liu, and A. S. Nowick, Phys. Rev. Lett. **67**, 1559 (1991).

[34] A. Seeger, P. Lunkenheimer, J. Hemberger, A. A. Mukhin, V. Y. Ivanov, A. M. Balbashov, and A. Loidl, J. Phys.: Condens. Mater. **11**, 3273 (1999).

[35] G. Williams and D. C. Watts, Trans. Faraday Soc. **66**, 80 (1970).

[36] C. C. Homes, T. Vogt, S. M. Shapiro, S. Wakimoto, and A. P. Ramirez, Science **293**, 673 (2001).

[37] J. Wu, C. W. Nan, Y. Lin, and Y. Deng, Phys. Rev. Lett. **89**, 217601 (2002).

[38] H. G. Reik and D. Heese, J. Phys. Chem. Solids **28**, 581 (1967).

[39] D. Emin, Phys. Rev. B **48**, 13691 (1993).

[40] A. V. Puchkov, T. Timusk, M. A. Karlow, S. L. Cooper, P. D. Han, and D. A. Payne, Phys. Rev. B **52**, R9855(R) (1995).

[41] R. Arita, T. Miyake, T. Kotani, M. van Schilfgaarde, T. Oka, K. Kuroki, Y. Nozue, and H. Aoki, Phys. Rev. B **69**, 195106 (2004).

[42] S. Mildner, J. Hoffmann, P. E. Blöchl, S. Techert, and C. Jooss, Phys. Rev. B **92**, 035145 (2015).

[43] S. Ciuchi and S. Fratini, Phys. Rev. B **79**, 035113 (2009).

[44] I. G. Austin and N. F. Mott, Adv. Phys. **18**, 41 (1969).

[45] H. Holloway, Phys. Rev. B **37**, 874 (1988).

[46] S. Fratini and P. Quémerais, Eur. Phys. J. B **14**, 99 (2000).

[47] S. Fratini and P. Quémerais, Eur. Phys. J. B **29**, 41 (2002).

[48] G. Iadonisi, V. Mukhomorov, G. Cantele, and D. Ninno, Phys. Rev. B **76**, 144303 (2007).

[49] L. Baldassarre, A. Perucchi, E. Arcangeletti, D. Nicoletti, D. Di Castro, P. Postorino, V. A. Sidorov, and S. Lupi, Phys. Rev. B **75**, 245108 (2007).

[50] L. V. Gasparov, D. B. Tanner, D. B. Romero, H. Berger, G. Margaritondo, and L. Forro, Phys. Rev. B **62**, 7939 (2000).

[51] A. Perucchi, L. Baldassarre, A. Nucara, P. Calvani, C. Adamo, D. G. Schlom, P. Orgiani, L. Maritato, and S. Lupi, Nano Lett. **10**, 4819 (2010).